THE PROTEIN SOCIETY

Structural features of interfacial tyrosine residue in ROBO1 fibronectin domain-antibody complex: Crystallographic, thermodynamic, and molecular dynamic analyses

Taisuke Nakayama,[1†] Eiichi Mizohata,[1†] Takefumi Yamashita,[2] Satoru Nagatoishi,[3] Makoto Nakakido,[3] Hiroko Iwanari,[4] Yasuhiro Mochizuki,[4] Yuji Kado,[1] Yuki Yokota,[1] Reiko Satoh,[1] Kouhei Tsumoto,[3] Hideaki Fujitani,[2] Tatsuhiko Kodama,[2] Takao Hamakubo,[4]* and Tsuyoshi Inoue[1]*

[1]Structural Physical Chemistry, Division of Applied Chemistry, Graduate School of Engineering, Osaka University, Osaka, Japan

[2]Laboratory for Systems Biology and Medicine, Research Center for Advanced Science and Technology, The University of Tokyo, Tokyo, Japan

[3]Medical Proteomics Laboratory, The Institute of Medical Science, The University of Tokyo, Tokyo, Japan

[4]Department of Quantitative Biology and Medicine, Research Center for Advanced Science and Technology, The University of Tokyo, Tokyo, Japan

Received 12 September 2014; Revised 2 December 2014; Accepted 4 December 2014
DOI: 10.1002/pro.2619
Published online 9 December 2014 proteinscience.org

Abstract: ROBO1, fibronectin Type-III domain (Fn)-containing protein, is a novel immunotherapeutic target for hepatocellular carcinoma in humans. The crystal structure of the antigen-binding fragment (Fab) of B2212A, the monoclonal antibody against the third Fn domain (Fn3) of ROBO1, was determined in pursuit of antibody drug for hepatocellular carcinoma. This effort was conducted in the presence or absence

Abbreviations: CDR, complementarity-determining region; Fab, antigen-binding fragment of antibody; Fn, fibronectin Type-III domain; Fn3, the third Fn domain of human ROBO1; Fv, variable fragment of antibody; IPTG, isopropyl-β-D-thiogalactopyranoside; ITC, isothermal titration calorimetry; LY50A, mutant in which Tyr is substituted with Ala at position 50 of the light chain of Fv; mAb, monoclonal antibody; MD, molecular dynamics; scFv, single-chain Fv; sROBO1, soluble ROBO1; TEV, tobacco etch virus.

Additional Supporting Information may be found in the online version of this article.

[†]Taisuke Nakayama and Eiichi Mizohata contributed equally to this work.

Makato Nakakido's current address is Department of Medicine, BSD, The University of Chicago, 5812 S. Ellis Avenue, Chicago, IL 60637.

Accession Numbers: The Protein Data Bank accession codes for the atomic coordinates and structure factor amplitudes of Fn3-Fab complex and free Fab reported in this article are 3WIH and 3WII, respectively.

Grant sponsors: Molecular Dynamics for Antibody Drug Development (MDADD) project, Funding Program for World-Leading Innovative R&D on Science and Technology (FIRST) program, JSPS; JST ERATO Lipid Active Structure Project; Japan Synchrotron Radiation Research Institute (JASRI) SACLA Project; MEXT SPIRE Supercomputational Life Science Grant numbers: hp120297, hp130006, hp140228; JSPS KAKENHI Grant numbers: 25282230, 24770096, 22550152.

*Correspondence to: Tsuyoshi Inoue; Structural Physical Chemistry, Division of Applied Chemistry, Graduate School of Engineering, Osaka University, 2-1 Yamadaoka, Suita-shi, Osaka 565-0871, Japan. E-mail: inouet@chem.eng.osaka-u.ac.jp or Takao Hamakubo; Department of Quantitative Biology and Medicine, Research Center for Advanced Science and Technology, The University of Tokyo, #34, 4-6-1 Komaba, Meguro-ku, Tokyo 153-8904, Japan. E-mail: hamakubo@qbm.rcast.u-tokyo.ac.jp

of the antigen, with the chemical features being investigated by determining the affinity of the antibody using molecular dynamics (MD) and thermodynamics. The structural comparison of B2212A Fab between the complex and the free form revealed that the interfacial $Tyr^{L}50$ (superscripts L, H, and F stand for the residues in the light chain, heavy chain, and Fn3, respectively) played important roles in Fn3 recognition. That is, the aromatic ring of $Tyr^{L}50$ pivoted toward $Phe^{F}68$, forming a CH/π interaction and a new hydrogen bond with the carbonyl O atom of $Phe^{F}68$. MD simulations predicted that the $Tyr^{L}50$-$Phe^{F}68$ interaction almost entirely dominated Fab-Fn3 binding, and Ala-substitution of $Tyr^{L}50$ led to a reduced binding of the resultant complex. On the contrary, isothermal titration calorimetry experiments underscored that Ala-substitution of $Tyr^{L}50$ caused an increase of the binding enthalpy between B2212A and Fn3, but importantly, it induced an increase of the binding entropy, resulting in a suppression of loss in the Gibbs free energy in total. These results suggest that mutation analysis considering the binding entropy as well as the binding enthalpy will aid in the development of novel antibody drugs for hepatocellular carcinoma.

Keywords: antigen–antibody interaction; antibody engineering; crystallography; molecular dynamics; thermodynamics

Introduction

Antibody-based cancer therapy has become well established over the past decades and is one of the most important strategies for treating tumor patients.[1,2] Anticancer antibody drugs have been developed to target cell surface antigens that are overexpressed in human cancer cells relative to normal tissue. Early anticancer antibody drugs utilize immunological mechanisms to kill cancer cells. This strategy requires that many target molecules are present on cancer cells and that multiple antibodies are bound to each cell. Antibodies conjugated with radioisotopes or cytotoxic agents also defeat cancer cells effectively, but there is considerable invasion into normal tissue. Currently, pretargeting strategies are proposed for advanced therapeutics, which aim to selectively deliver radioisotopes or prodrugs to tumors.[3,4] This approach typically requires distinct and separate steps. In the first step, for example, a streptavidin-conjugated antibody component targets the tumor, followed by clearance of the residual antibody. Subsequently, a biotinylated radioisotopes or prodrug is administered and delivered selectively to the tumor site. At each stage, achieving high-affinity binding between the antigen and antibody is imperative in expanding detection limits, extending dissociation half-lives, decreasing drug dosages, and increasing drug efficacy.[5]

The antibody has an antigen-binding fragment (Fab) which contains six hypervariable complementarity-determining regions (CDRs) that present a large contiguous surface for antigen recognition.[6] The database of natural antibody sequences has revealed that, whereas the compiled CDR sequences are highly diverse, there are clear biases for particular amino acids. That is, as tyrosine is highly abundant in antigen-binding sites, it is believed that the interfacial Tyr residues have a dominant role in antigen recognition.[7–9] Therefore, amino acid residues on the surface of the antigen recognition site can direct the affinity, specificity, or stability of the antigen–antibody reaction. In addition, the antibody performance can be improved by site-directed mutagenesis of the CDRs, incorporation of additional CDRs, emerging conformational change upon binding, rearrangement of interfacially trapped water molecules, and a trade-off of protein solvent with protein–protein interactions by polar and charged side chains.[10] Likewise, to develop antibody drugs for pretargeting, it is necessary to accomplish humanization of antibodies to suppress their immunogenicity[11] and to reduce molecular size while maintaining specificity, affinity, and lowered immunogenicity.[10] In this regard, a crystal structure of an antigen–antibody complex can indicate which residues should be mutated to upgrade preliminary antibodies to antibody drugs with the desired properties.

The human homologue of the *Drosophila* roundabout (robo) gene, *ROBO1*, encodes an axon guidance receptor, which is defined as a novel subfamily of the immunoglobulin superfamily.[12] As *Drosophila* robo functions as a gatekeeper controlling midline crossing,[12–14] ROBO1 is a member of the neural cell adhesion molecule family. Recently, ROBO1 also represents a novel immunotherapeutic target and a sensitive serological marker for hepatocellular carcinoma because the *ROBO1* gene expression is upregulated in hepatocellular carcinoma. Actually, ROBO1-positive cells were observed in more than 80% of hepatocellular carcinoma.[15]

ROBO1 contains five repeats of immunoglobulin (Ig) domains, three repeats of fibronectin Type-III (Fn) domains, a transmembrane domain, and an intracellular tail.[13] Among these domains, the structure of the first Ig domain has been determined by X-ray crystallographic analysis as the complex with the second leucine-rich repeat domain of SLIT2,[16] a known ligand for ROBO1. ROBO1/SLIT2 signaling has been shown to be involved in cancerous angiogenesis.[17] The third Fn domain of ROBO1 (Fn3) is located closest to the transmembrane region, but its function remains unknown. Typically, Fn domains are estimated to be present in about 2% of all human proteins

Table I. *Data Collection and Refinement Statistics for B2212A Fab and ROBO1 Fn3-Fab Complex*

	B2212A Fab	ROBO1 Fn3-Fab complex
Data collection		
X-ray source	BL41XU, SPring-8	BL44XU, SPring-8
Wave length (Å)	1.00000	0.90000
Detector	Rayonix MX225HE	Rayonix MX225HE
Space group	$P2_1$	$C2$
Unit cell dimension (Å)	$a = 41.82$, $b = 136.49$, $c = 77.51$	$a = 159.47$, $b = 102.60$, $c = 97.24$
(°)	$\alpha = \gamma = 90.0$, $\beta = 91.86$	$\alpha = \gamma = 90.0$, $\beta = 127.57$
Resolution (Å)	50.0–1.60 (1.66–1.60)[a]	50.0–1.70 (1.76–1.70)
No. of frames	450	225
Observations	1,688,795	1,629,875
Unique reflections	109,771	128,266
Completeness (%)	95.9 (90.4)	94.4 (91.9)
Redundancy	3.3 (2.3)	2.9 (2.3)
$I/\sigma(I)$	17.6 (5.1)	15.4 (3.9)
R_{merge} (%)[b]	10.7 (24.9)	3.5 (21.5)
Refinement statistics		
Resolution (Å)	14.9–1.60 (1.64–1.60)	15.0–1.70 (1.75–1.70)
No. of reflections	107,141 (10,309)	127,984 (12,400)
No. of water molecule	663	1,094
R_{work} (%)[c]	18.5 (19.1)	18.9 (26.9)
R_{free} (%)[d]	23.0 (28.1)	23.6 (33.9)
Mean B-factor (Å^2)	30.9	10.8
RMSD, Bond length (Å)	0.008	0.003
RMSD, Bond angles (°)	1.229	0.774
Ramachandran plot		
Most favored (%)	96.4	97.3
Allowed (%)	2.7	2.0
Outliers (%)	0.9	0.7

[a] Numbers in parentheses refer to the shell of highest resolution.
[b] $R_{merge} = \Sigma\ |I - \langle I \rangle| / \Sigma\ I$, where I is the observed intensity of a measured reflection, and $\langle I \rangle$ is the mean intensity of that reflection.
[c] $R_{work} = \Sigma\ ||F_o| - |F_c|| / \Sigma\ |F_o|$.
[d] $R_{free} = R$ factor calculated for 5% of data omitted from refinement calculations.

and found in organisms as evolutionarily distant as bacteriophages.[18] Moreover, Fn domain has a stable framework structure and consequently a high thermostability, which is utilized as a scaffold for the generation of stable proteins in the protein engineering.[19] Therefore, in ROBO1, Fn domains may contribute to stabilizing the extracellular region and the interaction with SLIT2.

In this study, we elucidated the crystal structure of the Fab fragment of B2212A (the specific antibody against human ROBO1 Fn3 domain), in the presence or absence of the antigen at 1.7 and 1.6 Å resolution, respectively, to uncover the structural features of Fn3 as well as to understand the recognition mechanism of B2212A antibody. Consequently, the structural comparison of the complexed and free forms of Fab revealed that the interaction between Fab and Fn3 was almost fully relying on the interfacial Tyr residue of Fab. Furthermore, from the results of molecular dynamics (MD) simulations and isothermal titration calorimetry (ITC), we discussed the thermodynamic features between antigen and antibody (as single-chain variable fragment, scFv) and the structural clues for molecular design of antibodies that display high-affinity binding.

Results

Overall structure of ROBO1 Fn3-B2212A Fab complex

The crystal structures of B2212A Fab were determined by X-ray crystallographic analysis in the presence or absence of Fn3 domain of human ROBO1 at resolutions of 1.7 and 1.6 Å, respectively, (Table I).

The final electron density map is well resolved for most of the complex with the exception of residues 31–35 and 83–85 of the Fn3 domain that are associated with weak electron density (i.e., disordered). However, the crystal structure allowed the interactions between Fn3 and Fab to be examined in atomic detail. A total of 1669 Å^2 (15.3%) of the solvent-accessible surface was buried in the interface between Fn3 and Fab: 804 Å^2 on Fn3, 508 Å^2 on the heavy chain of Fab, and the remaining 357 Å^2 on the light chain.

The B2212A Fab fragment showed the typical immunoglobulin fold. The overall structure of the framework regions was very similar to that of the structure of anti-gp41 Fab NC-1 (PDB ID code 3OZ9), which was used as a starting model for the

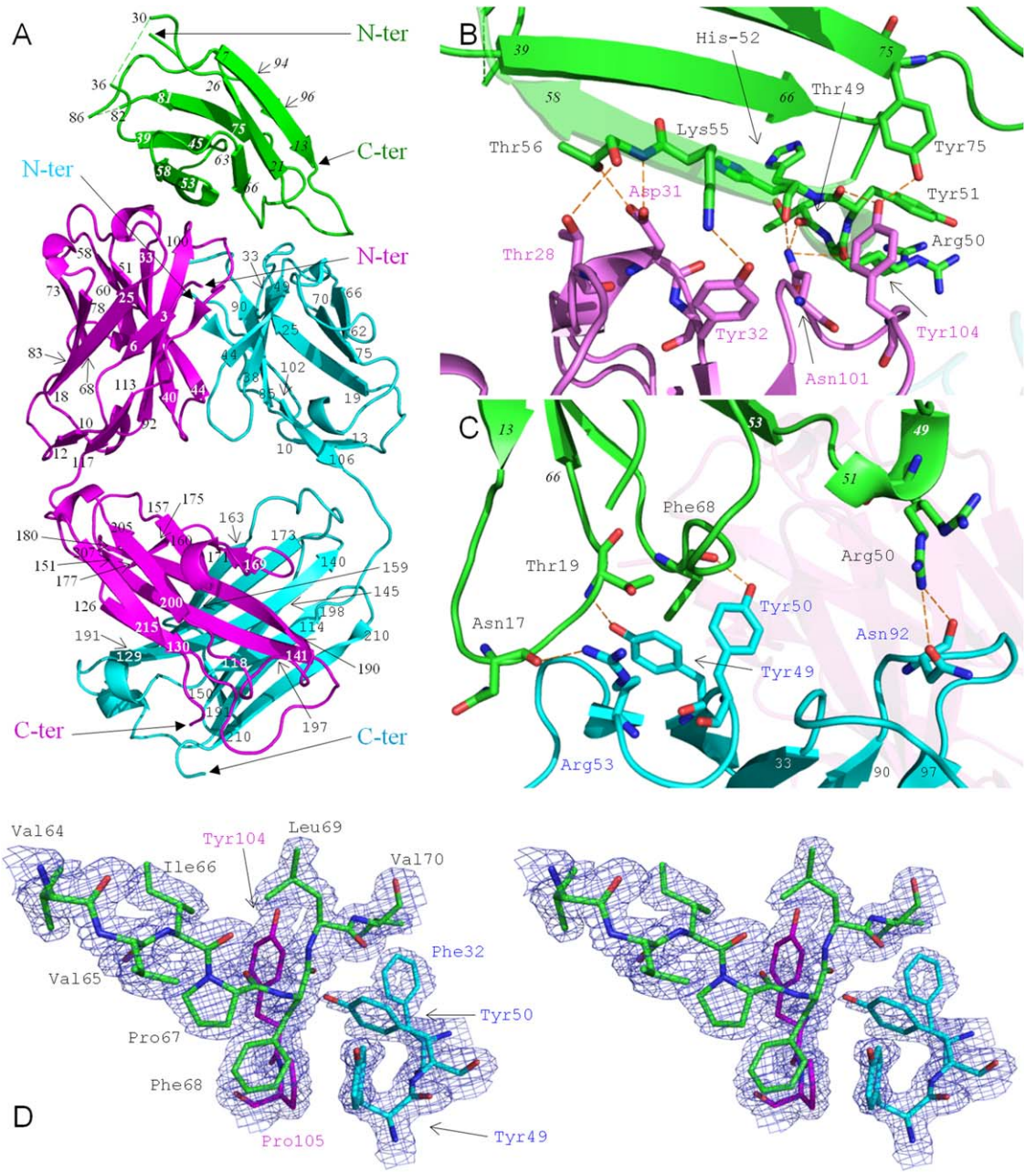

Figure 1. The complex of ROBO1 Fn3-B2212A Fab as determined by X-ray crystallographic analysis. Fn3 is shown in green with the heavy and light chains of Fab in magenta and cyan, respectively. (A) Whole structure of the complex. (B) Expanded view of the interface between Fn3 and the heavy chain of Fab, viewing the complex in panel A from the left side. (C) Expanded view of the interface between Fn3 and the light chain, viewing the complex in panel A from behind. Potential hydrogen bonds are shown as orange dashed lines. The Fn3 residues participating in hydrogen bonds are labeled in black, and those of Fab heavy and light chains in magenta and blue, respectively. (D) Stereo view of the hydrophobic cluster of Fn3 and the associating residues of Fab with the electron density map displayed at the level of 1.5 Å. Overall, assigned numbers depict the amino acid positions of the starting and the end points of each β-strand. See also Supporting Information Figure S1.

molecular replacement method. The root mean square deviation (RMSD) for 212 equivalent whole C^{α} atoms of each whole Fab was 1.6Å, but that for 103 equivalent C^{α} atoms in the variable region was 0.69 Å as the result of structural refinement. The differences between the crystal structures of the Fab complex and the free form were described.

ROBO1 Fn3 also exhibited the typical Fn domain fold [Fig. 1(A)]. The structure of Fn3 consisted of seven β-strands, which form a sandwich of two antiparallel β-sheets, one containing three strands and the other four strands. The RMSD for 88 equivalent C^{α} atoms between ROBO1 Fn3 and the 10th Fn domain of human fibronectin[20] was 1.2 Å, which was first determined by the crystal

Table II. *Residues Forming Hydrogen Bonds Between ROBO1 Fn3 and B2212A Fab in the Complex*

	B2212A-Fab		Fn3 domain		
	Residue	Atom	Residue	Atom	Distance (Å)
Light chain	Tyr49	OH	Thr19	N	3.0
	Tyr50	OH	Phe68	O	2.6
	Arg53	NH1	Asn17	O	3.4
	Asn92	O	Arg50	NH2	3.1
	Asn92	OD1	Arg50	NH2	3.5
Heavy chain	Thr28	OG1	Thr56	O	3.6
	Asp31	OD2	Thr56	N	2.7
	Asp31	OD1	Thr56	OG1	2.7
	Tyr32	OH	Lys55	NZ	3.1
	Asn101	ND2	Thr49	O	3.1
	Asn101	ND2	Arg50	O	3.2
	Asn101	ND2	His52	O	3.0
	Tyr104	OH	Tyr51	O	2.6
	Tyr104	OH	Tyr75	OH	2.6

structure of the mammalian Fn domain (PDB ID code 1FNA).

ROBO1 Fn3-B2212A Fab interface

The Fn3 epitope for B2212A Fab consisted of residues coming from distant parts of the linear sequence, but these residues were made contiguous by the folding of the protein. Mainly, the β-sheet spanning residues 49–56 of Fn3 bound with the heavy chain and several parts of loop regions spanning residues 17–19 and 68–75 associated with the light chain [Fig. 1(B,C) and Supporting Information Fig. S1]. On the contrary, only four CDRs among six participated in the interaction with Fn3. Namely, the second and third CDRs of the light chain (CDR-L2 and CDR-L3, respectively) and the first and third CDRs of the heavy chain (CDR-H1 and CDR-H3, respectively), made 14 hydrogen bond contacts with Fn3 [Fig. 1(B,C), Table II].

The surface of Fn3 interacting with B2212A Fab was not noticeably concave. However, there was a protrusion of the Phe^F68 side chain that penetrated into the small cavity in Fab and formed a CH/π interaction. In detail, the Phe^F68 side chain located in hydrophobic cluster spanning residues 64–70 (Val-Val-Ile-Pro-Phe-Leu-Val) was embedded in a hydrophobic surface consisting of Tyr^L49, Tyr^L50, Tyr^H104, and Pro^H105 [Fig. 1(D)].

Structural changes of B2212A Fab on binding of ROBO1 Fn3

To investigate the structural changes of B2212A Fab on binding of Fn3, the crystal structure of the free form of B2212A Fab was superimposed on the Fn3-complexed structure. No major conformational changes occurred in the structure of the B2212A Fab on complex formation [Fig. 2(A)]. Comparison of variable region between the complex and the free form of Fab gave a RMSD of 0.55 Å, corresponding to the C^α atoms. Importantly, the averaged distances between the corresponding C^α carbon atoms in CDR-L1 and L2 were calculated to be 0.8 and 1.3 Å, respectively (Supporting Information Table S1). Significant differences were also found for the side chain. Notably, on binding of Fn3 the aromatic ring of Tyr^L50 was rotated by 92° around the C^α—C^β bond to form a hydrogen bond with the carbonyl O atom of Phe^F68, while Tyr^L50 made a van der Waals interaction with Phe^L32 in the free form [Fig. 2(B)]. In fact, the electron density map corresponding to the side chain of Tyr^L50 showed two alternative conformations in the complexed form. Tyr^L50 was predominantly associated with Phe^F68, while the electron density showed that the OH group of Tyr^L50 was directed to Phe^L32 in the free form [Fig. 2(C)].

MD simulations

To investigate the interactions between the antigen and the antibody in more detail, we conducted MD simulations of the Fn3 complex and the B2212A Fv in physiological saline. The MD simulations led to the calculation that the interaction energy between Fn3 and Fv was −498 kJ/mol, which was considerably smaller than that of a typical example of antigen–antibody complexes (e.g., HEL and HyHEL10 is −745 kJ/mol).

The residue of Fn3 that had the highest interaction energy with B2212A was Phe^F68 (−83 kJ/mol), followed by Arg^F50 and Thr^F56 (−52 and −47 kJ/mol, respectively). The interaction energies of Tyr^F51, His^F52, Lys^F55, and Val^F70 in Fn3 exceed −20 kJ/mol (Table III). These results may indicate that both the hydrophobic cluster from Val^F64 to Val^F70 and the region from Thr^F49 to Thr^F56 in the third loop play an important role in the epitope. Also, Asn^F17 and Thr^F19 were observed to have a large interaction with B2212A. Interestingly, Phe^F68 interacted most strongly with Tyr^L50 (Table IV) producing the characteristic structural change, as shown earlier.

To investigate the function of Tyr^L50 in antigen recognition, we computationally constructed LY50A mutant Fv and performed the MD simulations under the same conditions as those used for the wild-type B2212A Fv. As a result, LY50A mutation led to a decreased binding interaction by +37 kJ/mol (Table III). Although Phe^F68 and Arg^F50 further reduced the binding interaction (+22 and +6.0 kJ/mol, respectively), Lys^F55 and Thr^F56 gained binding interaction (−7.5 and −22 kJ/mol, respectively). These results may indicate that the global structural change of the antigen–antibody interface was induced by the LY50A mutation; however, most of the important residue pairs were retained except for the interaction of the replaced Tyr^L50 (Table IV). Only the two Fn3 residues change the interaction pairs. One was Asn^F17, which

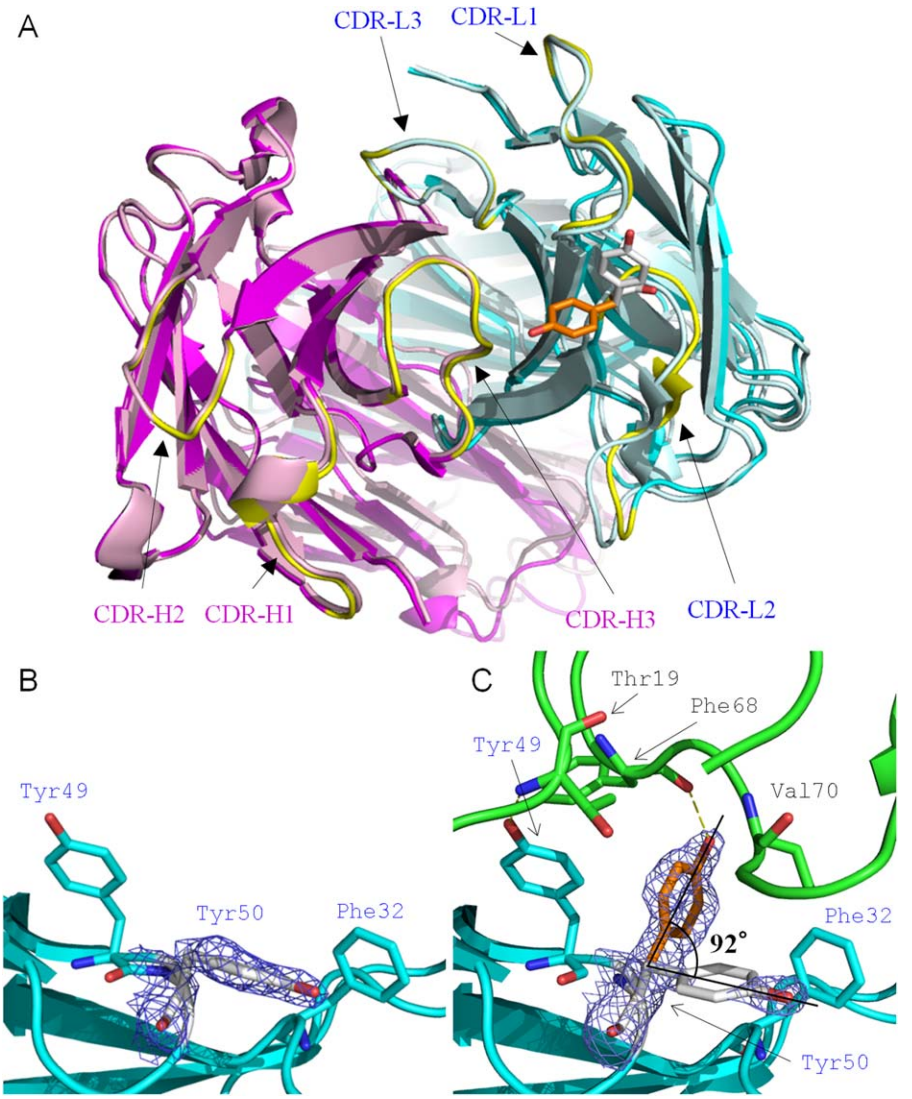

Figure 2. Conformational changes in B2212A Fab on binding of ROBO1 Fn3. Fn3, the heavy and light chains of Fab are shown in green, magenta and cyan, respectively. (A) Top surface of B2212A-Fabs in complexed (dark colored) and uncomplexed form (light colored), in which two conformational states of Fab are superimposed such that the RMSD between their C^{α} atoms of the variable region (amino acid positions 10–118 in the heavy chain and 10–106 in the light chain) are minimized. The loops colored in yellow show all six CDRs in the complex structure between B2212A Fab and Fn3. Aromatic sticks depict the location of $Tyr^{L}50$ on the top surface of Fab. (B) and (C) The states of the side chains of $Tyr^{L}50$ in the free and the complexed forms of Fab with the electron density map resolved at an σ level of 1.5 Å, respectively. Potential hydrogen bonds are presented as yellow dashed lines. The residues participating in interaction between Fn3 and the light chain are labeled in black and blue, respectively with arrows. Overall, the aromatic ring of $Tyr^{L}50$ associating with Fn3 is distinguished by its orange color.

decreased the interaction with $Arg^{L}53$, and increased the interaction with $His^{L}55$ and $Ser^{L}56$. The other was $His^{F}52$, which lost interaction with $Asn^{H}101$ but strengthened interaction with $Tyr^{H}104$.

Thermodynamic interactions between sROBO1 and B2212A scFvs

To uncover the role of $Tyr^{L}50$ residue in the antigen recognition, the wild-type and LY50A-mutated B2212A scFvs, and sROBO1 were prepared. The interaction between B2212A scFvs and sROBO1 with ITC was subsequently measured (Fig. 3; Table V).

The binding enthalpy (ΔH) for the interaction between the LY50A mutant scFv and sROBO1 (−38.9 kJ/mol) was compared to that between the wild-type scFv and sROBO1 (−49.3 kJ/mol). This demonstrated that the increase of $\Delta\Delta H$ was +10.4 kJ/mol by substituting $Tyr^{L}50$ with $Ala^{L}50$. In opposition, the entropic term ($T\Delta S$) also increased by +4.2 kJ/mol (+0.84 to +5.02 kJ/mol). As a result, LY50A did not lead to a large difference in Gibbs free energy ($\Delta\Delta G$) compared with the wild-type scFv-sROBO1 interaction (+5.8 kJ/mol). The net result was that the binding constant for LY50A was as much as one-tenth of that for the wild type.

Table III. *Top 10 Ranking of the ROBO1 Fn3 Interaction Energies on Wild-Type B2212A Fab Binding, and Their Changes With Respect to LY50A Mutant Fab*

	Potential energy (kJ/mol)						
	Wild type			LY50A			
Fn3 residue	Electrostatic potential	Lennard-Jones potential	Total	Electrostatic potential	Lennard-Jones potential	Total	ΔTotal
Phe68	−37.7	−45.3	−83.0	−7.99	−52.9	−60.8	−22.2
Arg50	−22.3	−29.2	−51.5	−25.8	−19.7	−45.5	−6.00
Thr56	−43.5	−3.84	−47.4	−62.7	−6.86	−69.5	22.1
Asn17	−27.1	−20.0	−47.0	−27.1	−21.3	−48.4	1.40
Lys55	−35.6	−8.35	−43.9	−41.4	−10.0	−51.4	7.50
His52	−28.9	−7.98	−36.9	−35.6	−12.4	−48.0	11.1
Tyr51	−17.8	−19.0	−36.8	−1.82	−22.5	−24.3	−12.5
Thr19	−11.7	−12.9	−24.6	−18.3	−7.75	−26.0	1.40
Val70	−0.478	−20.3	−20.8	1.17	−10.3	−9.08	−11.7
Ile53	−0.793	−17.0	−17.8	−1.19	−14.6	−15.7	−2.10
whole	−257	−241	−498	−234	−227	−461	−37

Discussion

In this article, we report the crystal structure of the Fn domain of mammalian ROBO1 complexed with its antibody B2212A Fab. Structural comparison of B2212A Fab between the complexed and the free form revealed that the $Tyr^{L}50$ residue rotated by

Table IV. *Significant Interaction Pairs Between Fn3 and B2212A Fv*

	Complex formed with									
	Wild-type Fv					LY50A Fv				
Residues of B2212A Fv	Residues of ROBO1 Fn3									
$Tyr^{L}50$[a]	Phe68 (−29)	Val70 (−10)	Leu69 (−7)	Pro71 (−6)		(No significant interaction for $Ala^{L}50$)				
$Arg^{L}53$	Asn17[b] (−16)	Thr19 (−7)				Thr19 (−8)				
$Leu^{L}54$	Asn17 (−16)					Asn17 (−15)				
$Tyr^{L}49$	Thr19 (−16)	Phe68 (−13)				Thr19 (−18)	Phe68 (−15)	Leu69 (−11)		
$Asn^{L}92$	Arg50 (−9)					Arg50 (−8)				
$His^{L}55$						Asn17[b] (−12)	Phe68 (−6)			
$Ser^{L}56$						Asn17[b] (−7)				
$Asp^{H}31$	Thr56 (−41)	Lys55 (−34)				Thr56 (−55)	Lys55 (−41)			
$Asn^{H}101$	His52[b] (−26)	Arg50 (−13)	Thr49 (−8)			Arg50 (−19)				
$Tyr^{H}104$	Tyr51 (−21)	Tyr75 (−13)	Phe68 (−12)	His52[b] (−9)	Ile53 (−8)	His52[b] (−16)	Phe68 (−14)	Tyr51 (−9)	Ile53 (−8)	Leu69 (−6)
$Val^{H}103$	Arg50 (−11)	Tyr51 (−8)				Tyr51 (−8)	Arg50 (−7)			
$Pro^{H}105$	Phe68 (−11)					Phe68 (−12)				
$Tyr^{H}102$	Arg50 (−10)					Arg50 (−6)				
$Tyr^{H}32$	Lys55 (−9)					Lys55 (−9)				
$Asp^{H}107$	Phe68 (−7)					Phe68 (−7)				
$Thr^{H}28$	Thr56 (−6)					Thr56 (−13)				

The interaction pairs that exceed −6 kJ/mol are given.
[a] Interaction of $Ala^{L}50$ was calculated for the LY50A mutant.
[b] $Asn^{F}17$ and $His^{F}52$ were altered their interaction priorities by Ala-substitution of $Tyr^{L}50$.
Parentheses indicate the corresponding interaction energies (kJ/mol).

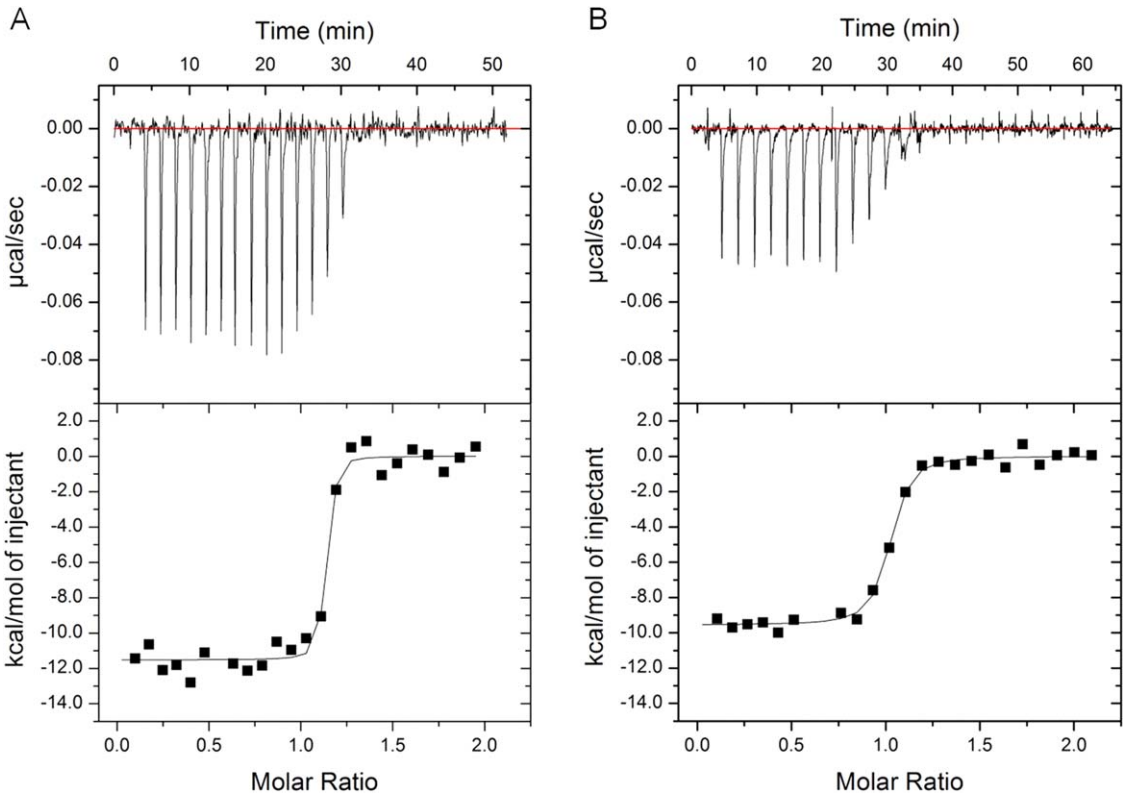

Figure 3. Thermodynamic analyses of the interactions between B2212A scFvs and sROBO1 as determined by ITC. Raw thermograms (lower) and titration curves (upper) for wild-type scFv-sROBO1 (A) and LY50A-sROBO1 (B) at 25°C, pH 7.4, are shown. The base line obtained by titrating each scFv solution (5.0 μ*M*) with buffer was subtracted from the thermogram obtained by titrating the corresponding scFv solution with a sROBO1 solution (54.4 μ*M*).

more than 90° with amino acids in other CDR loops showing no noticeable motion on binding of the ROBO1 Fn3 domain. In other words, there was no significant change in the interface other than $Tyr^{L}50$ residue. Therefore, to derive the structural clue for molecular design to develop antibody drugs, we almost focused on clarifying the role of $Tyr^{L}50$ of B2212A Fab on Fn3 recognition.

During the formation of antigen–antibody complexes, local conformational changes of both molecules have often been observed, leading to high specificity and affinity.[21,22] It can be supposed that induced fitting of an antibody to its antigen is critical for high specificity and affinity. Induced fitting can be achieved by small movements of side chains, by structural modifications such as deformation of CDR loops, or by a change in the relative orientation of variable domains. In this case, configuration of the side chain of $Tyr^{L}50$ plays a crucial role in the antigen–antibody interaction, even though the overall RMSD between the complex and the free form of Fab is very small value of 0.55 Å. The hallmark of this reorganization results in the $Tyr^{L}50$ aromatic ring being rotated around the axis of the C^{α}—C^{β} bond, generating a new hydrogen bond with the carbonyl O atom of $Phe^{F}68$ on binding of Fn3 (Fig. 2). Meanwhile, the MD simulations suggested that the hydrophobic residues, $Tyr^{L}49$, $Tyr^{L}50$, $Tyr^{H}104$, and $Pro^{H}105$, contribute mainly during complex formation (Tables III and IV). These results suggest that B2212A Fab gained binding energy by rotating the $Tyr^{L}50$ aromatic ring toward the $Phe^{F}68$ residue, thus picking up a hydrogen bonding interaction.

Table V. *Thermodynamic Parameters of the Interactions Between sROBO1 and B2212A scFvs*

	WT	LY50A
K_d (n*M*)	19 ± 4.0	238 ± 109
K_a ($\times 10^8\ M^{-1}$)	5.6 ± 1.2	0.53 ± 0.3
ΔG (kJ/mol)	−49.7 ± 0.4	−43.9 ± 1.3
ΔH (kJ/mol)	−49.3 ± 0.8	−38.9 ± 1.3
$T\Delta S$ (kJ/mol)	0.84 ± 1.7	5.02 ± 0.4

Experimental procedures are described in the text. All data are shown by the mean ± SEM of at least three independent measurements. The abbreviations used are as follows: K_d, dissociating constant; K_a, binding constant; ΔH, ΔS, ΔG, changes in binding enthalpy, entropy, and Gibbs energy, respectively.

In general, binding interfaces are closely packed[6,23] and systematic mutagenesis studies have revealed which "hot spots" tend to be intolerant of mutations. Remarkably, amino acid substitutions outside of the hot spots are typically tolerated.[24] A

significant bias in the amino acid composition has been found among interface residues.[25] For example, these regions are particularly enriched in Tyr, which plays an important role for antigen recognition because the aromatic ring of Tyr is capable of the formation of CH/π and π/π interactions in addition to forming a hydrogen bond.[9,26] As demonstrated in the case of HEL/HyHEL-10, there is an interfacial Tyr dictating the correct ternary structure of variable regions in both the light and heavy chains and the antigen.[8] Interestingly, 50th residue of the light chain of HyHEL-10 is Tyr, which is important on binding of HEL. In addition, the $Tyr^{L}50$ was comparably conserved (52% frequency) in 55 antiprotein antibody crystal structures (κ light chain of IgG2a in particular).[27] Taken together, these results suggest that the $Tyr^{L}50$ is significant for the antigen–antibody interaction, not only including antigen recognition, but also for stabilization of the antigen–antibody complex.

To verify the role of the $Tyr^{L}50$ residue in the recognition of Fn3, the mutation analysis by using LY50A was performed by ITC to investigate whether ΔG and ΔH were altered. Consequently, the ITC experiments demonstrated that LY50A led to a drastic increase in the binding enthalpy ($\Delta\Delta H$; +10.4 kJ/mol; Table V). This result was also predicted by the MD simulations as described earlier. Unexpectedly, there was relatively small increase in Gibbs energy ($\Delta\Delta G$; +5.8 kJ/mol), because the loss of binding enthalpy was compensated by the gain of binding entropy ($T\Delta\Delta S$; +4.2 kJ/mol). That is, the Ala residue provided a large energy gain for $T\Delta S$ to compensate the loss of ΔG. Ordinarily, a drug design directs a drug molecule to bind to its target with high affinity and selectivity. As the binding affinity is a combined function of ΔH and ΔS, extremely high affinity requires that both terms contribute favorably to binding.[28] It is often occurred that the phenomenon of enthalpy/entropy compensation rears its head as a problem. For example, in protease inhibitors, the enthalpy gain achieved by additional hydrogen bonding is compensated completely by an entropy loss, resulting in no affinity change.[29] In this case, there was only a small decrease in the affinity of LY50A for sROBO1, which was compensated by an entropy gain. It seems likely that most of the important residue pairs were retained with the global structural change of Fn3-B2212A interface, even though Ala-substitution disrupted the hydrogen bond and hydrophobic interaction (i.e., π/π and CH/π interactions; Tables III and IV). Therefore, we propose that Ala-substitution is a useful way for surveying not only hot spots but also potentially important residues contributing favorably to binding.

In this study, ITC experiments were also performed with Fn3 as well as sROBO1 as antigen samples. The properties of Fn3 showed the same tendency with those of sROBO1 but were not significant (Supporting Information Fig. S2 and Table S2). These differences can be attributed to the hydration states of the two Fn3 types. The Fn3 domain of sROBO1 is located appropriately with an accurate conformation, and the accessibility of water molecules is restricted due to the ternary structure of sROBO1. However, the free Fn3 fragment is small and naked, presenting a situation where water molecules can be freely accessed. Consequently, the rate of local hydration of the free Fn3 will be higher than that of Fn3 accompanying sROBO1. An antibody must sacrifice binding energy in displacing water molecules to interact with Fn3, most likely breaking hydrogen bonds in the process. In addition, sROBO1 is closely related to the endogenous molecule and relatively stable,[30] whereas the free Fn3 in aqueous solution also could be aggregated probably by the committing its hydrophobic residues [Fig. 1(D)]. Therefore, in discussing the thermodynamics of antigen recognition of B2212A, the data from the ITC experiments with sROBO1 were our main focus.

Herein, the interaction energy of each complex, wild-type Fv-Fn3 and LY50A Fv-Fn3, were calculated as the sum of the electrostatic potential and the Lennard-Jones potential using MD simulations. The difference in the interaction energy between the two complex types ($\Delta\Delta H$) was largest with the LY50A. It is difficult to predict the value of ΔS using MD simulations. However, both MD simulations and thermodynamic experiments will be indispensable for molecular design of antibody drugs. With the object of structure-function relationship, the crystal structure analysis of LY50A Fab-Fn3 complex is also in progress. In the near future, according to the accumulated knowledge, experiences, and experimental data using these techniques, the MD simulations need to be able to make accurate predictions of ΔS with respect to the formation of the antigen–antibody complex. This will be aided by the development of improved MD algorithms and supercomputing power.

To develop antibody drugs suitable for pretargeting strategies for cancer, it is necessary to construct a scFv conjugated with immunogenicity-lowered streptavidin. In fact, our group has already succeeded in reducing immunogenicity of streptavidin (patent pending). Therefore, once a high-affinity scFv is designed, the antibody drug project will have to progress to the next step (i.e., pharmacokinetic studies). We expect that the antihuman ROBO1 Fn3 antibody will evolve into the magic bullet against hepatocellular carcinoma,[15] or other tumors involving SLIT2/ROBO1 signaling (e.g., angiogenesis)[17] in the near future.

Materials and Methods

Chemicals

All chemicals were purchased from Wako Pure Chemical Ind. (Osaka, Japan) unless indicated otherwise.

Preparation of ROBO1 Fn3 domain

The cDNA fragment of human ROBO1 Fn3 domain (residues 741–837) was cloned into pTAT6 expression vector (generously gifted by Dr. Marco Hyvonen, University of Cambridge, UK). The Fn3 domain was expressed as a hexahistidine-tagged N-terminal thioredoxin A fusion protein via a linker containing a tobacco etch virus (TEV) protease recognition site. The protein was produced in *Escherichia coli* strain BL21Star (DE3; Life Technology, Rockville, MD). Cells were grown at 37°C up to an OD_{600} value of 0.6, and protein induction was performed by adding 0.4 m*M* isopropyl-β-D-thiogalactopyranoside at 15°C for 24 h. The cells were harvested by centrifugation, resuspended in a lysis buffer [50 m*M* phosphate buffer (pH 7.4) and 500 m*M* NaCl], and disrupted by EmulsiFlex-C3 (Avestin, Ottawa, Canada). The crude extract was centrifuged at 100,000*g* for 30 min at 4°C and the supernatant was subjected to affinity purification with Ni-NTA superflow (Qiagen, Hilden, Germany) resin. The hexahistidine-tagged protein was eluted with an imidazole gradient, and the eluted sample was diluted to 5 mg/mL or less. TEV protease was added (1/100 wt/wt ratio) to the sample, and the solution was dialyzed against gel filtration buffer [20 m*M* Tris-HCl (pH 8.0) and 600 m*M* NaCl] at 4°C. A HisTrap HP (GE Healthcare, Little Chalfont, UK) affinity column was used to remove the hexahistidine-tagged thioredoxin and the uncleaved fusion protein away from free Fn3, which was then concentrated and subjected to gel filtration chromatography using a Superdex 75 (GE Healthcare) column. The purified Fn3 protein was concentrated to 5 mg/mL and stored at −80°C. Protein concentration was determined spectrophotometrically based on absorbance at 280 nm using the calculated molar extinction coefficient of the protein.

Preparation of B2212A Fab fragment and ROBO1 Fn3-Fab complex

The monoclonal antibody (mAb) against human ROBO1 Fn3, clone B2212A, was generated as shown in Supporting Information. The ammonium sulfate fraction of B2212A mAb was adsorbed on HiTrap Protein G (GE Healthcare) column. The antibody was subsequently eluted with 100 m*M* glycine-HCl (pH 2.7) and then dialyzed against a dialysis buffer [100 m*M* sodium phosphate buffer (pH 7.0), 150 m*M* NaCl, and 2 m*M* ethylenediaminetetraacetic acid]. Papain was added (1/100 wt/wt ratio) in the presence of 40 m*M* freshly prepared L-cysteine and digestion was carried out at 37°C for 3 h. The reaction was quenched by the addition of iodoacetamide at a final concentration of 30 m*M*. The digestion mixture was dialyzed against 20 m*M* Tris-HCl (pH 8.0), loaded on HiTrap Q (GE Healthcare) anion exchange column, and eluted with NaCl gradient. The purified Fab fragment was mixed with Fn3 in 1:1.2 molar ratio and incubated for 1 h at 20°C. The Fn3-Fab complex was separated from excess Fn3 by gel filtration chromatography with a Superdex 75 column. The purified Fn3-Fab complex was concentrated to 5 mg/mL and stored at −80°C. Protein concentration of the complex was determined spectrophotometrically.

Crystallization

For the crystallization experiments, the purified Fn3-Fab complex was concentrated to 5 mg/mL. All crystallization screening kits used were purchased from Hampton Research (Aliso Viejo, CA). The clusters of thin plate-like crystals were grown using the sitting-drop vapor diffusion method within 2–3 weeks under the following conditions: equal volumes (0.5 μL) of the Fn3-Fab complex and precipitant, 25.5% (wt/vol) polyethylene glycol (PEG) 4000, 0.085 *M* sodium citrate tribasic dehydrate (pH 5.6), 0.17 *M* ammonium acetate, and 15% (vol/vol) glycerol (condition 9, Crystal Screen Cryo) were mixed and equilibrated at 20°C. In the case of a free Fab: 25% (wt/vol) PEG 4000, 0.1 *M* sodium acetate trihydrate (pH 4.6) and 0.2 *M* ammonium sulfate (condition 20, Crystal Screen), or 22% (wt/vol) PEG 3,350, 0.1 *M* sodium citrate tribasic dehydrate (pH 5.5), and 0.10% (wt/vol) *n*-octyl β-D-glucopyranoside (condition 25, PEGRx 2).

Structure determination and refinement

X-ray diffraction data for free Fab and Fn3-Fab complex crystals were collected at 100 K on the beamlines BL41XU and BL44XU at the SPring-8 (Harima, Japan), respectively, using MX225-HE detector (Rayonix, Evanston, IL). The crystal was fished with a standard nylon loop and flash-cooled in a nitrogen-gas stream at 100 K. Crystals were cryoprotected in a reservoir solution supplemented with 30% (vol/vol) glycerol. Data processing and reduction were carried out with the *HKL-2000* program suite.[31] The structures of B2212A Fab and ROBO1 Fn3 domain were determined by molecular replacement using the program *MOLREP*[32] in the *CCP*4 program suite[33] with the structures of the Fab fragment of anti-gp41 Fab NC-1 (PDB ID code 3OZ9) and the third Fn domain of human Neogenin (PDB ID code 1X5H) as search models, respectively. There were two monomers in the crystals of free Fab and the Fn3-Fab complex per asymmetric unit, resulting in a solvent content of 42.4% ($V_M = 2.15$ Å^3/Da) and 49.5% ($V_M = 2.46$ Å^3/Da), respectively.

These values were within the frequently observed ranges for protein crystals. Structural refinements were carried out with the program *REFMAC* version 5.5.01[34] and *PHENIX* version 1.8.4.[35] The structures were visualized and manually modified with the *COOT* software.[36] The stereochemical configurations of the refined structures were validated with the program *PROCHECK*,[37] which showed that only 0.8% residues are in disallowed regions of a Ramachandran plot in the both crystal structures. The buried surface area was calculated with the program *PISA*[38] at the PDBe website. Interactions within the Fn3-Fab interface were assigned with the *CONTACT* program in the *CCP*4 suite or the *PISA* program. Data collection and refinement statistics are summarized in Table I.

MD simulations

Prior to MD simulations, the coordinates of the fragment of variable region of antibody (Fv) were extracted from the initial structure of the wild-type complex taken from the crystal structure in this work. We utilized *Discovery Studio* version 3.1 (Accelrys, San Diego, CA) to generate several missing residue coordinates (Fn3 residues from 31 to 35 and 83 to 85), and to computationally generate the mutant structure by replacing $Tyr^{L}50$ of the wild-type structure with Ala (LY50A). The MD simulations were performed for each of the wild-type Fv-Fn3 complex and LY50A Fv-Fn3 complex. The structure was energetically minimized after adding 20,547 water molecules, 63 Na^+ ions, and 60 Cl^- ions to reproduce the saline physiological environment. In this work, we used a modified version of the AMBER protein model,[39] and the TIP3P water model for describing the interaction of the solvated protein systems. Although the protein coordinates were restrained to those of the minimized structure, the water molecules and ions were equilibrated for 250 ps using a MD simulation. Subsequently, the positional restraints were removed, and three 400 ns MD trajectories were calculated with randomly generated initial velocities for each the wild type and LY50A complex, respectively. In all the simulations, the temperature and pressure were adjusted to 298 K and 1 atm with the Nose–Hoover thermostat and Berendsen barostat. For both the thermostat and the barostat, the relaxation time constants were set to 0.1 ps. To address the long-range coulombic interactions, the particle mesh Ewald method was used with a real space cutoff of 1 nm. The simulation time step was 2 fs. All chemical bond lengths were kept constant using the LINCS algorithm. Because the RMSD with respect to the crystal structure gradually increased for the first 100 ns, the latter 300 ns trajectories were used for the interaction energy analysis where the long-range electrostatic term was neglected. For systematic comparison, the same analyses were conducted for the hen egg lysozyme (HEL)-HyHEL10 complex (PDB ID code 2DQJ).[8] In this work, all MD trajectories were calculated using *GROMACS* version 4.5.5.[40]

ITC experiments

Prior to ITC experiments, wild type and LY50A mutant of B2212A scFvs and soluble ROBO1 (sROBO1) were prepared (See Supporting Information). Thermodynamic parameters of the interaction between B2212A scFv antibodies and its antigens were determined using MicroCal iTC200 system (GE Healthcare). The experimental conditions were as follows: in a calorimeter cell, the scFv fragments, at a concentration of 5–10 μM in phosphate-buffered saline [10 mM phosphate buffer (pH 7.4), 150 mM NaCl and 45 mM KCl], were titrated with 55.4–96.2 μM solution of antigens in the same buffer at 25°C. The antigen solution was injected 25 times. Thermograms were analyzed with *Origin* 7 software (GE Healthcare) after subtraction of the thermogram against a buffer background. The enthalpy change (ΔH) and binding constant (K_a) for the antigen–antibody interaction were directly obtained from the experimental titration curve fitted to a one-site binding isotherm. The dissociation constant (K_d) was calculated as $1/K_a$. The Gibbs free energy change ($\Delta G = -RT \ln K_a$) and the entropy change (ΔS $\Delta(-\Delta G + \Delta H)/T$) for the association were calculated from ΔH and K_a.

Acknowledgments

The authors are grateful to the staff for their excellent support during data collection on the BL41XU and BL44XU at SPring-8. The authors also thank Y. Hattori and M. Takeichi for secretarial assistance and K. Watanabe for technical assistance. This work was carried out under the Japanese research project Molecular Dynamics for Antibody Drug Development (MDADD), which is supported by the Cabinet Office, Government of Japan and the Japan Society for the Promotion of Science (JSPS) through the Funding Program for World-Leading Innovative R&D on Science and Technology (FIRST Program) initiated by the Council for Science and Technology Policy (CSTP). Author contributions: T.N. and E.M. constructed the systems for expression and purification of Fn3 and performed X-ray crystallography; H.I., Y.M., and T.H. provided antibody clone B2212A; R.S. performed Fab preparation; T.N. prepared Fn3-Fab complex; Y.K. and Y.Y. helped with experiments; T.Y. and H.F. performed molecular dynamics simulations; S.N., M.N., and K.T. performed thermodynamic analyses; E.M. and T.I. conceived and designed the study and analyzed data; T.N. wrote the manuscript with contributions from E.M., S.N., K.T., T.Y., H.F., T.H., and T.I.; T.K. supervised the MDADD project.

References

1. Carter P (2001) Improving the efficacy of antibody-based cancer therapies. Nat Rev Cancer 1:118–129.
2. Carter P, Smith L, Ryan M (2004) Identification and validation of cell surface antigens for antibody targeting in oncology. Endocr Relat Cancer 11:659–687.
3. Stoldt HS, Aftab F, Chinol M, Paganelli G, Luca F, Testori A, Geraghty JG (1997) Pretargeting strategies for radio-immunoguided tumour localisation and therapy. Eur J Cancer 33:186–192.
4. Chang CH, Sharkey RM, Rossi EA, Karacay H, McBride W, Hansen HJ, Chatal JF, Barbet J, Goldenberg DM (2002) Molecular advances in pretargeting radioimunotherapy with bispecific antibodies. Mol Cancer Ther 1:553–563.
5. Lippow SM, Wittrup KD, Tidor B (2007) Computational design of antibody-affinity improvement beyond in vivo maturation. Nat Biotechnol 25:1171–1176.
6. Mian IS, Bradwell AR, Olson AJ (1991) Structure, function and properties of antibody binding sites. J Mol Biol 217:133–151.
7. Fellouse FA, Wiesmann C, Sidhu SS (2004) Synthetic antibodies from a four-amino-acid code: a dominant role for tyrosine in antigen recognition. Proc Natl Acad Sci USA 101:12467–12472.
8. Shiroishi M, Tsumoto K, Tanaka Y, Yokota A, Nakanishi T, Kondo H, Kumagai I (2007) Structural consequences of mutations in interfacial Tyr residues of a protein antigen-antibody complex. The case of HyHEL-10-HEL. J Biol Chem 282:6783–6791.
9. Koide S, Sidhu SS (2009) The importance of being tyrosine: lessons in molecular recognition from minimalist synthetic binding proteins. ACS Chem Biol 4:325–334.
10. Chowdhury PS, Pastan I (1999) Improving antibody affinity by mimicking somatic hypermutation in vitro. Nat Biotechnol 17:568–572.
11. Carter P, Presta L, Gorman CM, Ridgway JB, Henner D, Wong WL, Rowland AM, Kotts C, Carver ME, Shepard HM (1992) Humanization of an anti-p185HER2 antibody for human cancer therapy. Proc Natl Acad Sci USA 89:4285–4289.
12. Brose K, Bland KS, Wang KH, Arnott D, Henzel W, Goodman CS, Tessier-Lavigne M, Kidd T (1999) Slit proteins bind Robo receptors and have an evolutionarily conserved role in repulsive axon guidance. Cell 96: 795–806.
13. Kidd T, Brose K, Mitchell KJ, Fetter RD, Tessier-Lavigne M, Goodman CS, Tear G (1998) Roundabout controls axon crossing of the CNS midline and defines a novel subfamily of evolutionarily conserved guidance receptors. Cell 92:205–215.
14. Li HS, Chen JH, Wu W, Fagaly T, Zhou L, Yuan W, Dupuis S, Jiang ZH, Nash W, Gick C, Ornitz DM, Wu JY, Rao Y (1999) Vertebrate slit, a secreted ligand for the transmembrane protein roundabout, is a repellent for olfactory bulb axons. Cell 96:807–818.
15. Ito H, Funahashi S, Yamauchi N, Shibahara J, Midorikawa Y, Kawai S, Kinoshita Y, Watanabe A, Hippo Y, Ohtomo T, Iwanari H, Nakajima A, Makuuchi M, Fukayama M, Hirata Y, Hamakubo T, Kodama T, Tsuchiya M, Aburatani H (2006) Identification of ROBO1 as a novel hepatocellular carcinoma antigen and a potential therapeutic and diagnostic target. Clin Cancer Res 12:3257–3264.
16. Morlot C, Thielens NM, Ravelli RB, Hemrika W, Romijn RA, Gros P, Cusack S, McCarthy AA (2007) Structural insights into the Slit-Robo complex. Proc Natl Acad Sci USA 104:14923–14928.
17. Wang B, Xiao Y, Ding BB, Zhang N, Yuan XB, Gui L, Qian KX, Duan S, Chen Z, Rao Y, Geng JG (2003) Induction of tumor angiogenesis by Slit-Robo signaling and inhibition of cancer growth by blocking Robo activity. Cancer Cell 4:19–29.
18. Fraser JS, Yu Z, Maxwell KL, Davidson AR (2006) Ig-like domains on bacteriophages: a tale of promiscuity and deceit. J Mol Biol 359:496–507.
19. Bloom L, Calabro V (2009) FN3: a new protein scaffold reaches the clinic. Drug Discov Today 14:949–955.
20. Dickinson CD, Veerapandian B, Dai XP, Hamlin RC, Xuong NH, Ruoslahti E, Ely KR (1994) Crystal structure of the tenth type III cell adhesion module of human fibronectin. J Mol Biol 236:1079–1092.
21. Davies DR, Cohen GH (1996) Interactions of protein antigens with antibodies. Proc Natl Acad Sci USA 93: 7–12.
22. Sundberg EJ, Mariuzza RA, Molecular recognition in antibody-antigen complexes. In: Janin J, Wodak SJ, Eds. (2002) Advanced in Protein Chemistry, Vol 61. Amsterdam: Elsevier, pp 119–160.
23. Lawrence MC, Colman PM (1993) Shape complementarity at protein/protein interfaces. J Mol Biol 234:946–950.
24. DeLano WL (2002) Unraveling hot spots in binding interfaces: progress and challenges. Curr Opin Struct Biol 12:14–20.
25. Lo Conte L, Chothia C, Janin J (1999) The atomic structure of protein-protein recognition sites. J Mol Biol 285:2177–2198.
26. Fellouse FA, Barthelemy PA, Kelley RF, Sidhu SS (2006) Tyrosine plays a dominant functional role in the paratope of a synthetic antibody derived from a four amino acid code. J Mol Biol 357:100–114.
27. Raghunathan G, Smart J, Williams J, Almagro JC (2012) Antigen-binding site anatomy and somatic mutations in antibodies that recognize different types of antigens. J Mol Recognit 25:103–113.
28. Freire E (2008) Do enthalpy and entropy distinguish first in class from best in class? Drug Discov Today 13: 869–874.
29. Lafont V, Armstrong AA, Ohtaka H, Kiso Y, Mario Amzel L, Freire E (2007) Compensating enthalpic and entropic changes hinder binding affinity optimization. Chem Biol Drug Des 69:413–422.
30. Seki M, Watanabe A, Enomoto S, Kawamura T, Ito H, Kodama T, Hamakubo T, Aburatani H (2010) Human ROBO1 is cleaved by metalloproteinases and gamma-secretase and migrates to the nucleus in cancer cells. FEBS Lett 584:2909–2915.
31. Ötwinowski Z, Minor W (1997) Processing of X-ray diffraction data collected in oscillation mode. Methods Enzymol 276:307–326.
32. Vagin A, Teplyakov A (2010) Molecular replacement with MOLREP. Acta Crystallogr D Biol Crystallogr 66: 22–25.
33. Winn MD, Ballard CC, Cowtan KD, Dodson EJ, Emsley P, Evans PR, Keegan RM, Krissinel EB, Leslie AG, McCoy A, McNicholas SJ, Murshudov GN, Pannu NS, Potterton EA, Powell HR, Read RJ, Vagin A, Wilson KS (2011) Overview of the CCP4 suite and current developments. Acta Crystallogr D Biol Crystallogr 67:235–242.
34. Murshudov GN, Skubak P, Lebedev AA, Pannu NS, Steiner RA, Nicholls RA, Winn MD, Long F, Vagin AA (2011) REFMAC5 for the refinement of macromolecular crystal structures. Acta Crystallogr D Biol Crystallogr 67:355–367.

35. Adams PD, Afonine PV, Bunkóczi G, Chen VB, Echols N, Headd JJ, Hung LW, Jain S, Kapral GJ, Grosse Kunstleve RW, McCoy AJ, Moriarty NW, Oeffner RD, Read RJ, Richardson DC, Richardson JS, Terwilliger TC, Zwart PH (2011) The Phenix software for automated determination of macromolecular structures. Methods 55:94–106.
36. Emsley P, Lohkamp B, Scott WG, Cowtan K (2010) Features and development of Coot. Acta Crystallogr D Biol Crystallogr 66:486–501.
37. Laskowski RA, MacArthur MW, Moss DS, Thornton JM (1993) PROCHECK: a program to check the stereochemical quality of protein structures. J Appl Crystallogr 26:283–291.
38. Krissinel E, Henrick K (2007) Inference of macromolecular assemblies from crystalline state. J Mol Biol 372: 774–797.
39. Fujitani H, Matsuura A, Sakai S, Sato H, Tanida Y (2009) High-level ab initio calculations to Improve protein backbone dihedral parameters. J Chem Theory Comput 5:1155–1165.
40. Hess B, Kutzner C, Van Der Spoel D, Lindahl E (2008) GROMACS 4: algorithms for highly efficient, load-balanced, and scalable molecular simulation. J Chem Theory Comput 4:435–447.